PERGAMON

Continental Shelf Research 18 (1998) 941–970

CONTINENTAL SHELF RESEARCH

Predicting ripple geometry and bed roughness under combined waves and currents in a continental shelf environment

Michael Z. Li*, Carl L. Amos

Geological Survey of Canada (Atlantic), Bedford Institute of Oceanography, Dartmouth, N.S. B2Y 4A2 Canada

Received 21 July 1995; received in revised form 15 August 1996; accepted 5 November 1996

Abstract

Waves, current and seabed response data collected by an instrumented tripod deployed on the Scotian Shelf during the winter of 1993/94 are analyzed to derive a ripple predictor for combined flows and to evaluate the applicability of existing ripple- and bedload-roughness algorithms under combined waves and current. Wave-dominant ripples developed during storms were generally higher and steeper than current-dominant ones. The ratio of the skin-friction wave shear velocity to that of the steady current, u_{*ws}/u_{*cs}, can be used to define the various types of ripples under combined flows. By comparing the measured ripple geometry and the predictions by existing ripple predictors, the wave-ripple predictors of Nielsen (1981), and Grant and Madsen (1982) are found to over-predict ripple height and ripple roughness for combined flows under the conditions of the present study. These methods also neglect the enhancement of shear stress at the ripple crest. A new empirical ripple predictor is proposed and it uses the combined shear velocity and the ratio u_{*ws}/u_{*cs} to predict the heights and wavelengths of ripples and their dynamic transition under combined flows. The effect of enhanced shear velocity at the ripple crest is also incorporated for the prediction of ripples in the weak-transport range.

A simplified logarithmic profile method and the values of the bedload shear velocity due to the combined grain size and bedload roughnesses are used to evaluate the applicability of various ripple- and bedload-roughness height algorithms under combined flows. While the ripple roughness height algorithm of Grant and Madsen (1982) is found to give good predictions of the total current shear velocity u_{*c} and apparent bottom roughness z_{0c}, the algorithm of Nielsen (1992), tends to underpredict both parameters. The bedload roughness algorithms of Nielsen (1992) and Li et al. (1997) are both found to give reasonable predictions under combined flows. The total bed roughness height under combined flows can be expressed as $k_b = 2.5D + 27.7\eta^2/\lambda + 170D(\theta_{cws} - \theta_{cr})^{0.5}$.

* Corresponding author.

PII S0278–4343(98)00034–X

1. Introduction

Accurate prediction of ripple geometry and bed roughness is crucial to the modelling of bottom boundary layer (BBL) dynamics and sediment transport since the ripple development and bed roughness variation directly control the magnitude of bed stress, skin friction/form drag partition, near bed velocity structure and vertical profiles of suspended sediment concentration (SSC) (Smith, 1997; Grant and Madsen, 1979, 1982; Glenn and Grant, 1987; Wiberg and Nelson, 1992; Li, 1994). Recent studies by Drake and Cacchione (1989), Vincent et al. (1991) and Li et al. (1996) also show that the change of ripple roughness with bed stress can significantly affect vortex shedding and sand resuspension in nearshore environments. Many studies have investigated ripple heights and wavelengths under waves (e.g., Inman, 1957; Carstens et al., 1969; Mogridge and Kamphuis, 1972; Dingler, 1974; Miller and Komar, 1980; Boyd et al., 1988). These studies indicate that as wave stress increases past the bedload threshold, both ripple height and length increase initially in this equilibrium range. During this stage, ripple length is proportional to the wave orbital diameter and ripple steepness is at the maximum and stays roughly constant. When wave stress is further increased, ripples first reach a maximum in their height and length and then enter a breakoff range. Ripple height decreases with the stress in this breakoff range, while ripple length stays roughly constant or only decreases slightly. When wave stress reaches the sheet flow criterion, ripples are washed out and upper-plane bed sheet flow occurs. Various models have been derived to predict ripple geometry for waves or combined flows (e.g., Nielsen, 1981; Grant and Madsen, 1982; Wiberg and Harris, 1994). However, these models are either based on laboratory data or valid for waves only, and have not been tested with combined-flow field data. Amos et al. (1988) have studied ripple generation under combined flows on the Scotian Shelf. Based on limited ripple measurements obtained from Duck, North Carolina and Scotian Shelf, Li et al. (1996) have proposed a modification of the Grant and Madsen's (1982) ripple predictor for combined flows. Nevertheless, a well-tested ripple predictor for the combined waves and current is not yet available.

When sediment transport occurs, the bed roughness is composed of three components: grain roughness, bedform (ripple) roughness and a roughness due to bedload transport. The bedload roughness directly affects the value of the total physical bed roughness and the prediction of shear stresses in the bottom boundary layer. Recent studies by Wilson (1988, 1989), Wiberg and Harris (1994) and Li et al. (1997) also show that the friction factor for sheet flow is correlated with the thickness of the bedload layer, and that the transport-related shear stress based on the sum of the grain size and bedload roughnesses should be used for predicting ripple geometry and thresholds of suspension and sheet flow conditions. Following the approach of Owen (1964), Smith and McLean (1977), Dietrich (1982) and Grant Madsen (1982) have developed expressions for bedload roughness, z_{0t}. Wiberg and Rubin (1989) have evaluated these expressions using unidirectional flume data under flat bed conditions. They found that while the predictions of Dietrich (1982) agree well with measurements, the other two methods significantly over-predict z_{0t}. Under waves, however, Nielsen (1992) shows that for a given shear stress, bedload roughness is about one order of magnitude higher than under unidirectional flows. A recent field study by Madsen et al. (1993) shows that bedload roughness height, k_{bt}, for a movable flat bed is about 15 times the median sediment grain diameter, D, though large scatter (2–60 times D) exists.

The objective of this paper is to analyze the wave, current and seabed response data collected with an instrumented tripod on the Scotian Shelf during the winter of 1992/93 in terms of the combined-flow bottom boundary layer model of Grant and Madsen (1986, GM86 here after). Several storms occurred during the field experiment. Thus the data cover a wide range of wave-current dynamic conditions. Various seabed states, ranging from no transport, through rippled bed, to suspension and sheet flows, were also observed with seabed photography. By comparing these field data with model predictions, we have evaluated existing models for the prediction of ripple geometry and derived a new ripple predictor for combined waves and current. Algorithms for predicting ripple and bedload roughness heights were also compared against the field measurements to provide an evaluation of the movable bed roughness under stormy combined-flow conditions.

2. Site description, data collection and analysis

2.1. The study site

The data presented here were collected on Sable Island Bank, Scotian Shelf, during the winter of 1992/93. Various instruments were deployed at several sites in this area to monitor wave/current dynamics and seabed responses. Fig. 1 shows the study area together with the Cohasset and Panuke development sites of the oil company LASMO Nova Scotia Limited. This paper deals only with the data collected from site 1.

Sable Island Bank is located about 180 km southeast of Nova Scotia. It is underlain by up to 30 m of Holocene sand moulded into a series of sand ridges (Amos and Nadeau, 1988). Semidiurnal tides dominate at the study site and the currents rotate in a clockwise fashion. Peak tidal flows are generally to the northeast or southwest and reach 35 cm/s. Waves generally are from the south and southwest due to sheltering by Sable Island. During the winter months from December to February, the annual highest significant wave heights are 6–8 m and the associated wave periods are 10–13 s. Summer significant wave heights are less than 2 m. Detailed reviews of the physical oceanography and surfacial geology are given in Mobil Oil Canada Ltd. (1983).

2.2. Instrumentation

The Geological Survey of Canada (GSC) instrumented tripod RALPH (Heffler, 1984) occupied site 1 (43°49.9′N, 60°50.1′W) from January 17 to February 14 of 1993 and collected simultaneous data on waves, currents, suspended sediment concentrations and seabed responses on this high-energy, storm-dominated continental shelf.

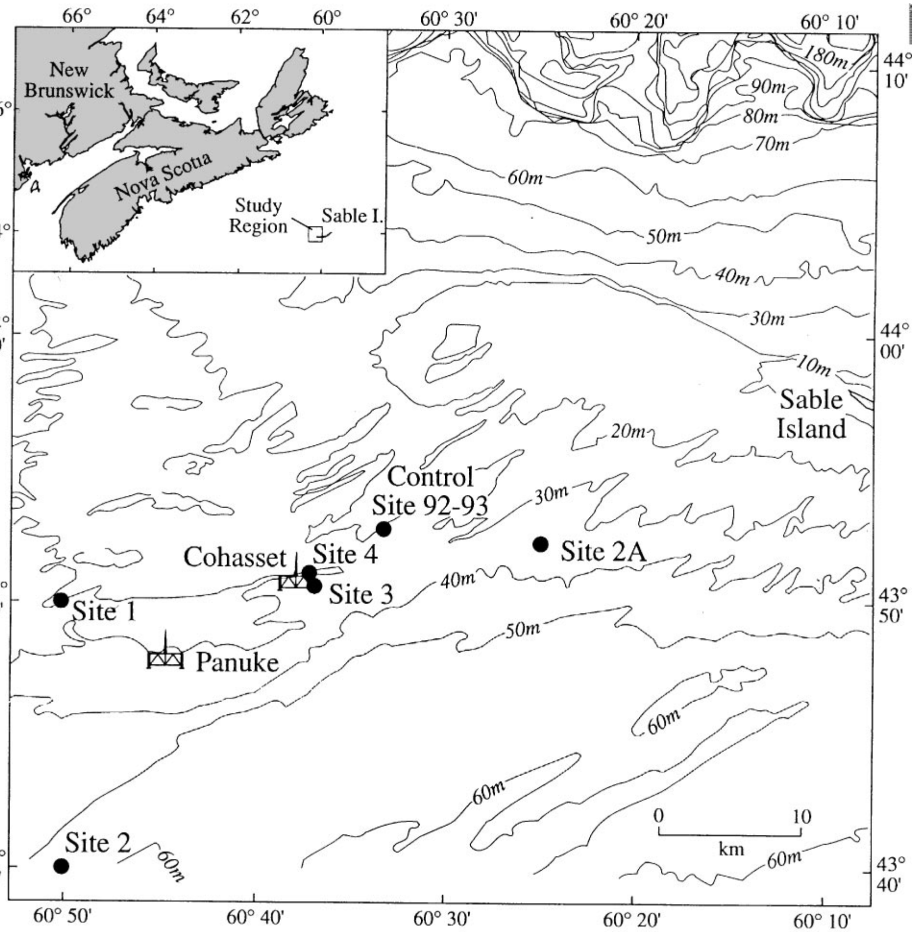

Fig. 1. The location map showing the study region on Sable Island Bank, Scotian Shelf. The Cohasset and Panuke development sites of LASMO Nova Scotia Limited are also illustrated.

The water depth at the deployment site was 39 m and the bottom sediment was well-sorted medium quartz sand with a median grain size $D = 0.34$ mm. RALPH for this study was equipped with two SACM acoustic current meters at heights of 50 and 100 cm above the sea floor, a Viatran 218-12 (250 psi) pressure transducer mounted 150 cm above the sea bed, two SeaTech optical transmissometers at 33 and 68 cm above the base and a KVH c-100 flux gate compass. A Minolta 601 time-lapse camera was installed at 150 cm above the bed with a flash at a closer distance (55 cm) from the bottom to obtain olique-angle seabed photographs. The camera was set to look down 20° from the vertical to give a field of view of 1.0 m by 1.5 m. A shadow bar was also installed on the tripod for ripple height and wavelength measurements. The data were recorded on an Onset Tattletale Model 6 data logger with a 20 Mbyte hard disk. All sensors were sampled every two hours for a period of 18 min at a frequency of 1 Hz. Two seabed photographs were taken with a 15 min separation for each sampling burst to monitor seabed responses. The current meters were calibrated in a tow tank before the deployment and were accurate to 3%. But the transmissometers were not calibrated and thus suspended sediment concentration is expressed as transmission percentages.

2.3. Data analysis

Each data burst was time averaged to obtain the mean water depth (h), mean current velocity (u_{100}) and direction (C_{dir}) 100 cm above the bed, and mean suspended sediment concentrations at 68 cm (SSC1) and 33 cm (SSC2) above the sea floor. The depth time series was de-meaned and used to compute the wave energy density spectrum. Wave period (T) was estimated from the peak of this spectrum and the significant wave height was obtained from $H_s = 4M_0^{0.5}$ where M_0 is the first moment of the wave energy density spectrum. For each velocity time series, the mean values of the x and y components were removed from each record to obtain wave orbital velocities. A least-square regression line was fitted to the scatter plot of the x and y components of the wave orbital velocities to determine the mean wave direction (W_{dir}). The median grain size D and burst-averaged h, u_{100}, C_{dir}, H_s, T, W_{dir} were then used with the combined-flow bottom boundary layer model of Grant and Madsen (1986) to compute various BBL parameters. The skin-friction shear velocities for current (u_{*cs}), waves (u_{*ws}) and combined wave-current (u_{*cws}) were obtained using the grain roughness only. Various ripple and bedload roughness height algorithms were substituted in the GM86 model to compute the total current shear velocity (u_{*c}) and the apparent bottom roughness (z_{0c}) in order to evaluate the applicability of these algorithms under combined flows.

The seabed images were digitized using a computer-controlled film advancing system, a photo enlarger and a Sony video camera. The photo enlarger projected each image directly onto the CCD of the video camera and the video signal was digitized using a Matrox frame-grabber in a PC. The digitized images were then analyzed using the Geographic Resources Assessment (GRASS) software for seabed classification, ripple geometry and ripple migration rate measurements. For each image, ripple wavelength (λ) was measured directly by referencing to the scale on the shadow bar. The flash-shadow bar geometry (Fig. 2a) gave a light incidence angle α of 49°. The distance between the shadow bar and the cast shadow at the ripple crest (L_c) and that at the ripple trough (L_t) were measured from the image (Fig. 2b). Ripple height (η) was then calculated from

$$\eta = (L_t - L_c)/\tan 49^\circ \tag{1}$$

The distances L_c and L_t measured in this way were distorted due to the projection of the bar onto the plane of the seabed as viewed by the camera, but it is the difference between them that determines η. This method was calibrated against known ripple heights and lengths. The errors of the estimated ripple length and height were less than 5% and 30%, respectively. Ripple crests were traced (digitized) in GRASS and the digitized images of the two seabed photos associated with each data burst

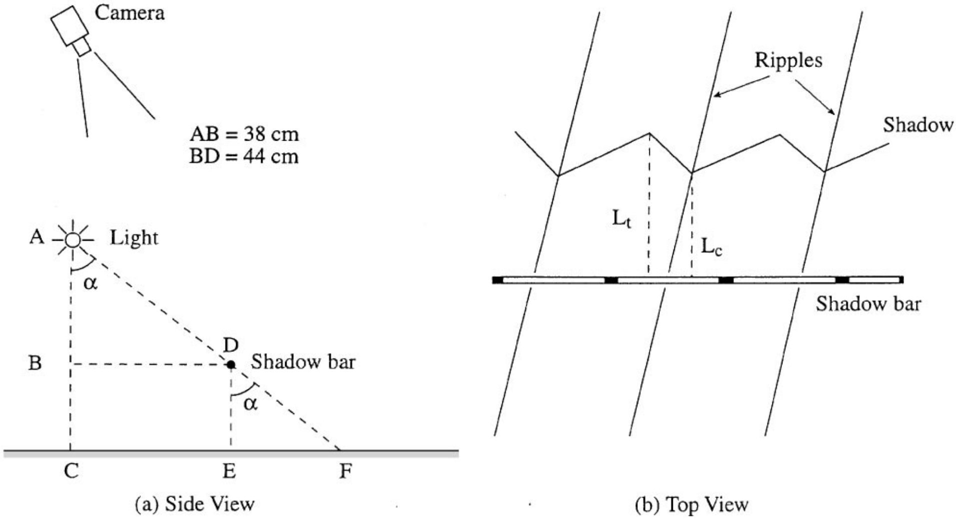

Fig. 2. A schematic diagram showing (a) the side view of the camera, flash-light and shadow bar set-up and (b) the top view of the shadow bar and cast shadow over ripples on seabed.

were overlain to obtain the ripple migration rate (R_m) . If the measured ripple migration rate was smaller than the GRASS digitization resolution (0.01 cm/min), *no motion* was defined as the bed state. If seabed images were clear and $R_m \geqslant 0.01$ cm/minute, *bedload transport* was defined. The general deterioration of image clarity marked the initiation of *saltation/suspension*, while the combination of strong image blurring and clearly-recognized flat bed indicated the upper-plane bed *sheet flow* conditions. Based on the descriptions of Allen (1968, 1982), Reineck and Singh (1975) and Amos et al. (1988), the seabed photos were visually observed to define the following bedform types: current-dominant ripples (C_w), wave-dominant ripples (W_c), combined wave-current ripples (W) and large wave ripples (LWR). C_w ripples are predominantly asymmetrical in shape with sharp brink points. Subordinate symmetrical wave ripples could occur intermittently in the troughs of the current ripples. W_c ripples are predominantly symmetrical in shape with sharp crests and bifurcations. Subordinate small current ripples could be seen in wave ripple troughs. WC ripples are composed of superimposed wave and current ripples with roughly equal magnitudes. Ripples with wavelengths more than 30 cm are defined as LWR in this study.

3. Results

3.1. The data

Time series of (a) u_{100}, (b) H_s, (c) T, and (d) SSC1 and SSC2 are plotted in Fig. 3 for the entire experiment. The time series of u_{100} in Fig. 3a shows that the peak tidal current velocity reached more than 35 cm/s during spring tides, but was generally less than 20 cm/s during neap tides. Fig. 3b and c show that three major storms (marked as SA, SD and SF) occurred during this experiment. Significant wave heights and wave periods were more than 2 m and 13 s, respectively, during these major storms. Three less energetic storms (marked as SB, SC and SE) also occurred, in which H_s were between 1 to 2 m and T was between 10 and 12 s. Two quiet periods (marked as QI and QII) occurred from days 4–6 and then from days 20–25. Under these periods, H_s was less than 0.5 m. During the extended non-storm period (days 20–25), u_{100} records in Fig. 3a clearly shows the semidiurnal tides. Under storm conditions (e.g., days 0–5), however, meterological forcing suppressed the tidal signal into nearly diurnal cycles. Time series of the suspended sediment concentrations at 33 and 68 cm above the seabed are shown in Fig. 3d as transmission%. All resuspension events occurred during storms. Several smaller suspension peaks also correlate well with the minor storms.

It is conventional to use the skin-friction shear velocity to determine the modes of sediment transport. Therefore the skin-friction combined shear velocities (u_{*cws}), predicted by the GM86 model using grain size roughness only, are compared with observed transport events in Fig. 4 to evaluate the thresholds of various transport modes under combined flows. Observed sediment saltation/suspension and upper-plane bed sheet flows are shown as triangles and circles, respectively. Large wave ripples were observed to develop immediately following the major storms (occurrences indicated by arrows in Fig. 4). Their geometry, formation mechanism and effects on BBL dynamics will be presented in a forthcoming publication. The two dashed lines represent the critical shear velocity for the initiation of bedload ($u_{*cr} = 1.51$ cm/s) and suspended load ($u_{*s} = 3.49$ cm/s), based on Miller et al. (1977) and Bagnold (1956), respectively. Fig. 4 shows that the skin-friction combined shear velocities for the observed saltation/suspension events (triangles) were significantly lower than the established threshold value of $u_{*s} = 3.49$ cm/s. Based on the wave-flume data of Manohar (1955), Komar and Miller (1975) have shown that the critical Shields parameter for sheet flow can be given by $\theta_{up} = 0.413D^{-0.396}$ in which D must be in mm. For $D = 0.34$ mm of the present study, the critical shear velocity for sheet flow will be $u_{*up} = 5.8$ cm/s. Apparently, u_{*cws} values for the observed sheet-flow events (circles in Fig. 4) are also much smaller than this established u_{*up} value. It is interesting to note that Sawamoto and Yamashita (1986) and Ribberink and Al-Salem (1994) have also observed sheetflow conditions below the established sheetflow threshold criterion, and that Drake and Cacchione (1992) find that the combined shear velocities based on one-tenth largest waves predicted sand suspension and bedform formation better than using the significant wave parameters (as we did here). The discrepancies shown in Fig. 4 support the findings in these studies. Li et al. (1997) have studied wave–current interaction and sediment transport prediction on Scotian Shelf. Following Wilson (1988) and Wiberg and Harris (1994), Li et al. suggest that when sediment is in transport, the sum of the grain size roughness and bedload roughness should be used to calculate a bedload shear velocity, u_{*cwb}. Good agreement can be achieved between u_{*s}, u_{*up} and the observed suspension and sheet-flow events when compared to this bedload shear velocity.

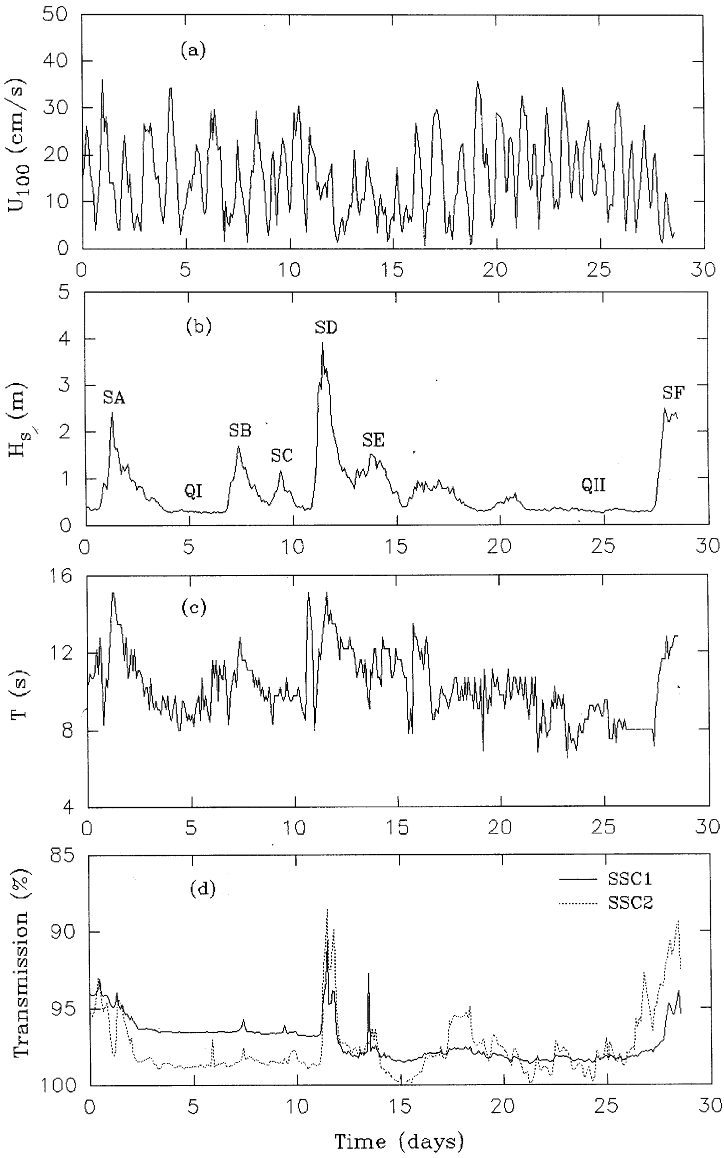

Fig. 3. Time series of RALPH data collected during the 1992/93 winter deployment on Sable Island Bank: (a) mean velocity 100 cm above the seabed (u_{100}, cm/s), (b) significant wave height (H_s, m), (c) peak spectral wave period (T, s), and (d) suspended sediment concentration (in transmission %) at 68 cm (SSC1) and 33 cm (SSC2) above seabed.

3.2. Ripple predication under combined flows

Fig. 5 shows the time series of (a) the measured ripple height, η, (b) ripple wavelength, λ, and (c) ripple steepness, η/λ. Zero values of η and λ on days 1, 11 and 28

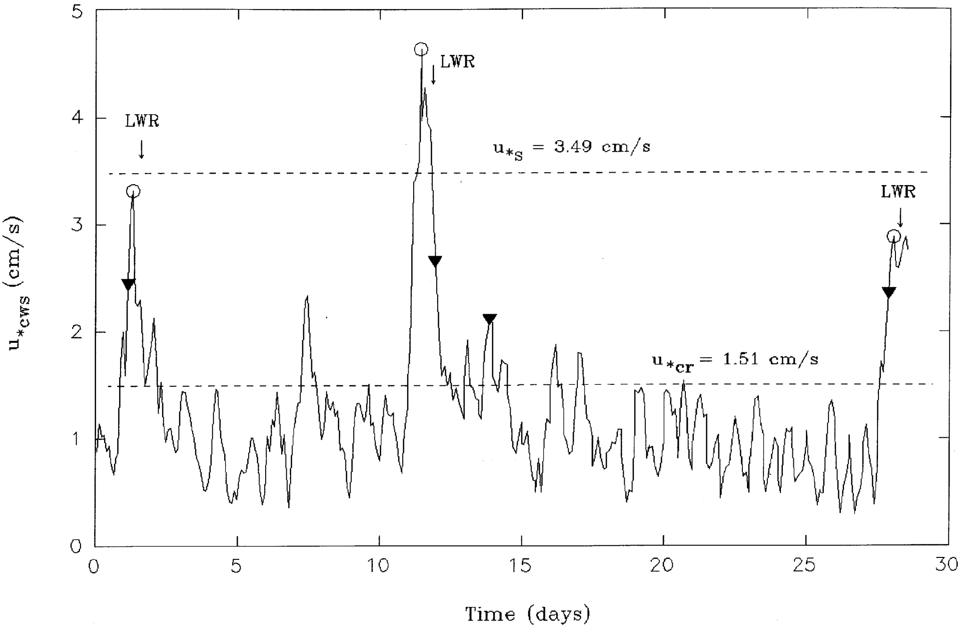

Fig. 4. Time series of the skin-friction combined shear velocity, u_{*cws} (cm/s), predicted by the Grant and Madsen (1986) BBL model. The dashed lines represent the critical shear velocities for bedload (u_{*cr} = 1.51 cm/s) and saltation/suspension (u_{*s} = 3.49 cm/s) transports respectively. Triangles and circles indicate observed saltation/suspension and sheet flow events. Large wave ripples (LWR) were also observed to immediately follow the sheet flow events in storms.

indicate upper-plane beds under sheet-flow conditions. Except for the large wave ripples (λ from 40–60 cm and η form 5–6 cm), the measured ripple heights generally range from 0.7 to 2.9 cm, ripple wavelength from 7 to 20 cm, and ripple steepness from 0.07 to 0.2. Comparing Fig. 5a and c with Fig. 3b indicates that larger and steeper ripples coincide with the storms. This suggests that higher ripple steepness prevails under wave-dominant conditions. Fig. 5a and b also show that LWR occur immediately following the sheet flow events during the three major storms.

The time series of the ratio of skin-friction wave shear velocity to skin-friction current shear velocity, u_{*ws}/u_{*cs}, is plotted in Fig. 6 with various ripple types marked by different symbols. The figure demonstrates that under combined flows, the ratio of u_{*ws}/u_{*cs} can be used to define various ripple types. On the average, current-dominant ripples (circles) generally occur when u_{*ws}/u_{*cs} is less than 0.75. When u_{*ws}/u_{*cs} is larger than 0.75 but less than 1.25, ripples are defined as combined wave–current ripples (squares). If u_{*ws}/u_{*cs} is between 1.25 and 2, the ripples can be classified as wave-dominant ripples (triangles) and pure wave ripples will occur only when u_{*ws}/u_{*cs} is larger than 2 (diamonds).

The more widely used ripple predictors are those of Nielsen (1981) and Grant and Madsen (1982). Wiberg and Harris (1994) have compared these two methods with wave ripple data and proposed a new method which produces essentially similar

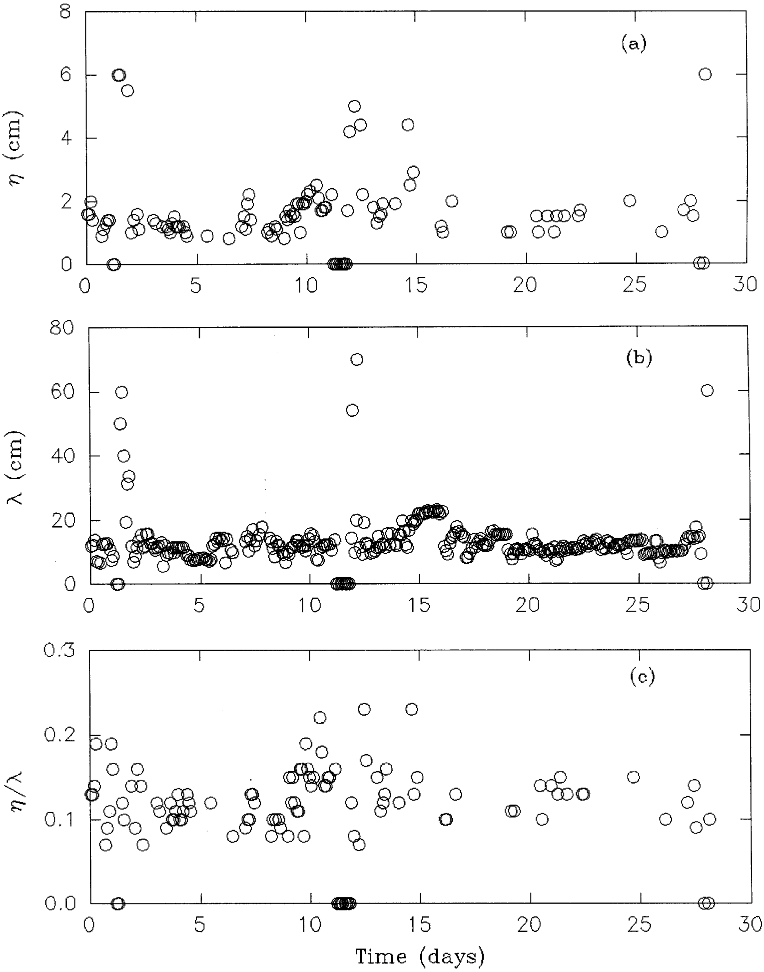

Fig. 5. Time series of (a) the measured ripple height η, (b) ripple wavelength λ, and (c) ripple steepness η/λ for the entire experiment.

predictions as that of the Nielsen method. In evaluating effects of ripple roughness on sand resuspension, Li et al. (1996) have suggested a modified Grant and Madsen equation for combined flows based on limited field measurements. The methods of Nielsen, Grant and Madsen, and Li et al. are briefly described below and are then evaluated against the measured ripple geometry data of this study to derive a ripple predictor for combined flows.

Based on field wave-ripple data of Inman (1957) and Dingler (1974), Nielsen (1981) obtained the following field wave-ripple predictor:

$$\lambda = A_{\mathrm{b}} \exp[693 - 0.37 \ln^8 M)/(1000 + 0.75 \ln^7 M)] \tag{2a}$$

$$\eta/\lambda = 0.342 - 0.34\theta_{\mathrm{ws}}^{0.25} \tag{2b}$$

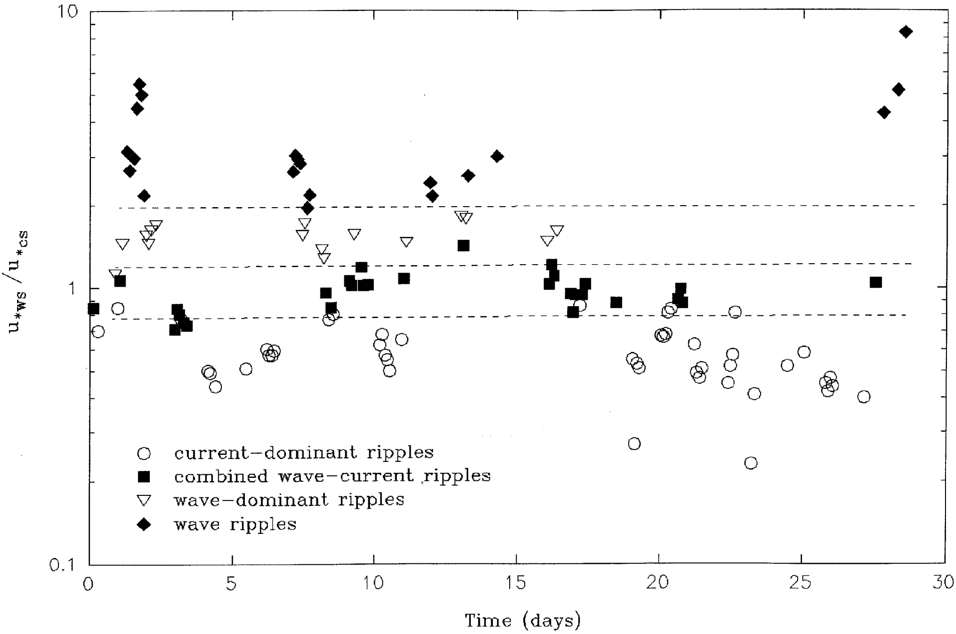

Fig. 6. The ratio of skin-friction wave shear velocity to skin-friction current shear velocity, u_{*ws}/u_{*cs}, plotted as a function of time for selected bursts. Circles represent observed current-dominant ripples, squares combined wave-current ripples, triangles wave-dominant ripples and diamonds wave ripples.

where A_b is the nearbed wave orbital amplitude, $\theta_{ws} = \rho u_{*ws}^2/(\rho_s - \rho)gD$ is the skin-friction wave Shields parameter and M is the wave mobility number defined as $\rho u_b^2/(\rho_s - \rho)gD$ in which u_b is the nearbed wave orbital velocity, D is the sediment grain size, g is the gravitation acceleration, ρ_s and ρ are the grain and fluid densities, respectively.

Based on the laboratory data of Carstens et al. (1969), Grant and Madsen (1982) derived expressions for wave-dominant ripples. They defined the critical Shields parameter for ripple breakoff as:

$$\theta_{bf} = 1.8\theta_{cr} S_*^{0.6} \tag{3}$$

where $\theta_{cr} = \rho u_{*cr}^2/(\rho_s - \rho)gD$ is the critical Shields parameter for bedload transport, and $S_* = (D/4v)\ [(\rho_s - \rho)gD/\rho]^{0.5}$ is a dimensionless sediment parameter (v, the fluid kinematic viscosity). When $\theta_{cr} < \theta_{ws} < \theta_{bf}$, ripples are in the equilibrium range and are predicted by

$$\eta = 0.22A_b(\theta_{ws}/\theta_{cr})^{-0.16} \tag{4a}$$

$$\lambda = 6.25\eta(\theta_{ws}/\theta_{cr})^{0.04} \tag{4b}$$

For $\theta_{ws} > \theta_{bf}$, ripples are in the breakoff range and are predicted by

$$\eta = 0.48 A_b S_*^{-0.8} (\theta_{ws}/\theta_{cr})^{-1.5} \tag{5a}$$

$$\lambda = 3.6 \eta S_*^{-0.6} (\theta_{ws}/\theta_{cr}) \tag{5b}$$

For $D = 0.34$ mm in this study, the breakoff Shields parameter θ_{bf} is 0.20 and the breakoff shear velocity u_{*bf} is 3.23 cm/s.

During a field experiment carried out by Wright et al. (1986) at Duck, North Carolina, ripple parameters were manually measured by divers at the beginning and/or the end of each field experiment. Using these limited ripple measurements, Li et al. (1996) found that the expression of Grant and Madsen (1982) over-predicts ripple heights and lengths, and the expression of Nielsen (1981) under-predicts ripples in the breakoff range. Li et al. (1996) proposed the following modification from the Grant and Madsen's (1982) method:

for $\theta_{cr} < \theta_{ws} < \theta_{bf}$,

$$\eta = 0.101 A_b (\theta_{ws}/\theta_{cr})^{-0.16} \tag{6a}$$

$$\lambda = 3.60 \eta (\theta_{ws}/\theta_{cr})^{0.04} \tag{6b}$$

and for $\theta_{ws} > \theta_{bf}$,

$$\eta = 0.356 A_b S_*^{-0.8} (\theta_{ws}/\theta_{cr})^{-1.5} \tag{7a}$$

$$\lambda = 3.03 \eta S_*^{-0.6} (\theta_{ws}/\theta_{cr}) \tag{7b}$$

Thirty-five bursts were chosen from the present study to evaluate the ripple predictors described above. For these bursts, both ripple height and length measurements were available. Ripple migration was also observed in these bursts, indicating that the ripples were active under the prevailing wave–current conditions. The measured η and λ of these bursts are listed in Table 1 together with the prevailing wave and current data. Bedload shear velocity u_{*cwb}, predicted by the GM86 model using the sum of the grain and bedload roughnesses when $u_{*cws} > u_{*cr}$, is also given in Table 1 (values of u_{*cws} were used if $u_{*cws} < u_{*cr}$). Time series of the measured ripple heights and the corresponding shear velocity u_{*cws} or u_{*cwb} for these bursts are plotted in Fig. 7a and c. Though these measured ripples are not all consecutive, they are connected with a solid line for purpose of clearer presentation. Since it is the ripple roughness height k_{br}, that is used in the BBL models, the measured ripple heights and lengths were used to obtain the 'observed' ripple roughness height as $k_{br} = 27.7\eta^2/\lambda$ (Grant and Madsen, 1982) and this observed ripple roughness height is plotted in Fig. 7b. The dashed lines in Fig. 7c represent the critical bedload and ripple breakoff shear velocities u_{*cr} and u_{*bf} respectively. Fig. 7 shows that except for two bursts, all our observed ripples are in the equilibrium range ($u_{*cwb} < u_{*bf}$). Therefore, ripple height generally increases with the combined shear velocity. When ripples are present, bed stress will increase from ripple trough to crest (Wiberg and Nelson, 1992; Li, 1994). The ripple-enhanced skin-friction shear velocity u_{*cwe} can be calculated from $u_{*cws}/(1 - \pi\eta/\lambda)$ according to Nielsen (1986). For some of the selected bursts (around days 5 and 10), the average skin-friction shear velocity u_{*cws} was less than the critical

Table 1
Measured ripple heights and ripple wavelengths with their wave and current input data to the Grant and Madsen (1986) model.

Day	h	H_s	T	u_{100}	ϕ_b	η	λ	η/λ	Type	u_{*cwb}
0.88	39.52	0.91	10.7	25.1	14	1.3	10.9	0.11	WC	2.01
0.96	39.12	0.88	10.2	36.2	21	1.4	11.8	0.12	WC	2.57
1.04	38.82	0.78	11.1	25.1	39	1.0	9.4	0.11	WC	1.76
2.04	38.97	1.32	11.1	24.2	3	1.7	12.1	0.14	W_c	3.02
2.13	38.76	1.04	12.2	18.0	29	1.4	8.9	0.16	W_c	2.12
2.29	39.59	0.97	12.2	16.0	51	1.6	11.4	0.14	W_c	1.67
3.04	39.15	0.54	10.7	25.0	21	1.4	11.4	0.12	WC	1.44
3.13	38.82	0.61	9.5	25.3	0	1.4	12.0	0.12	WC	1.44
4.13	38.96	0.28	9.2	27.7	44	1.2	11.4	0.10	C_w	1.21
4.21	38.76	0.31	9.8	34.0	55	1.2	11.6	0.11	C_w	1.46
4.29	39.09	0.32	8.5	34.3	45	1.2	11.5	0.10	C_w	1.44
4.38	39.77	0.31	8.0	25.0	61	1.2	9.0	0.13	C_w	1.03
4.46	40.03	0.32	8.0	20.6	19	1.0	9.0	0.12	C_w	0.93
5.46	39.98	0.30	8.5	22.2	18	0.9	7.7	0.12	C_w	1.01
6.46	39.87	0.28	10.7	25.0	27	0.8	9.9	0.08	C_w	1.19
7.29	38.71	1.49	11.6	9.1	71	1.9	13.1	0.14	W_c	2.43
7.38	39.08	1.70	12.8	11.2	47	2.2	15.4	0.14	W_c	3.66
7.46	39.74	1.51	11.6	23.1	19	2.2	14.3	0.15	W_c	3.57
8.21	39.09	0.76	10.2	16.2	19	1.0	13.2	0.08	WC	1.29
8.29	38.77	0.63	10.7	22.7	65	1.1	11.0	0.10	WC	1.28
8.38	38.95	0.64	9.8	29.4	80	1.0	8.6	0.11	WC	1.34
8.54	39.97	0.55	9.5	22.7	23	1.2	12.3	0.10	WC	1.26
9.13	39.77	0.71	9.8	18.8	54	1.4	11.5	0.12	WC	1.18
9.21	39.19	0.73	9.8	20.7	36	1.7	11.6	0.15	WC	1.33
9.29	38.78	0.88	10.2	13.5	1	1.5	12.3	0.12	W_c	1.33
9.54	39.81	0.76	9.8	16.5	29	1.9	11.9	0.16	WC	1.22
9.63	39.78	0.76	10.7	23.6	40	1.8	11.6	0.15	WC	1.62
10.54	39.77	0.34	8.5	25.8	44	1.7	12.7	0.14	C_w	1.13
11.13	39.91	1.31	10.7	20.7	49	2.0	13.9	0.14	WC	2.30
13.04	39.24	1.10	10.7	13.2	23	1.8	11.4	0.15	WC	1.70
13.21	39.73	1.02	11.6	13.6	53	1.3	11.5	0.11	WC	1.49
13.29	39.35	1.13	11.6	9.0	68	1.5	11.8	0.13	WC	1.47
14.04	39.03	1.20	10.7	12.2	40	1.9	14.3	0.13	WC	1.78
16.13	39.21	0.82	11.6	26.8	54	1.2	11.8	0.10	W_c	1.91
16.21	39.65	0.92	12.2	23.9	14	1.5	10.4	0.10	W_c	2.29

Note: h, mean water depth (m); H_s, significant wave height (m); T, peak spectral wave period (s); u_{100}, mean velocity at 100 cm above seabed (cm/s); ϕ_b, the angle between wave and current (degree); η, ripple height (cm); λ, ripple wavelength (cm); η/λ, ripple steepness; u_{*cwb}, bedload shear velocity (cm/s; $u_{*cwb} = u_{*cws}$ for $u_{*cws} < u_{*cr}$). Ripple types are as defined in the text.

shear velocity u_{*cr} but the ripple-enhanced shear velocity u_{*cwe} was larger than u_{*cr}, thus active ripples were observed for these bursts. The skin-friction wave shear velocity was used in various ripple predictors (Eqs. (2a)–(7b)) to predict ripple heights and ripple roughness heights. The predicted η and k_{br} by Nielsen (1981; long-dashed line), Grant and Madsen (1982; solid line) and the modified Grant and Madsen (1982) method of

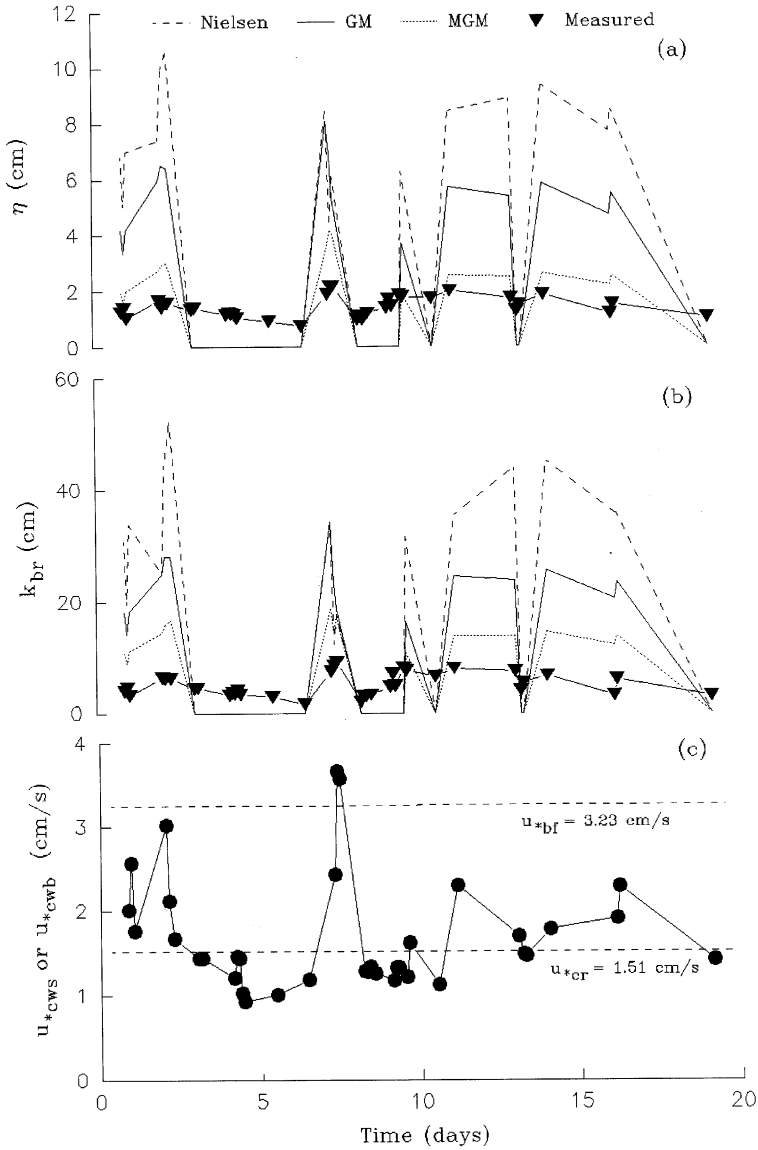

Fig. 7. Time series of (a) the measured ripple height η, (b) ripple roughness height k_{br} and (c) the skin-friction or bedload combined shear velocity (u_{*cws} or u_{*cwb}) for selected bursts. The ripple heights and ripple roughness heights predicted by Grand and Madsen (1982; GM, solid line), Nielsen (1981; dashed line) and the modified Grant and Madsen predictor of Li et al. (1996; MGM, dotted line) are also included for evaluation. The dashed lines in (c) are the threshold shear velocities for the initiation of bedload and ripple break-off.

Li et al. (1996; dotted line) are plotted in Fig. 7a and b to evaluate their applicability. Fig. 7 shows that for ripples in the equilibrium range, all three expressions over-predict η and k_{br}, though the modified Grant and Madsen method of Li et al. (1996)

seems to produce the best results. When $u_{*cws} < u_{*cr}$, all the methods predict no ripple formation. The enhancement of shear velocity by pre-existing ripples is not addressed by these methods.

The combined-flow ripple predictor proposed by Li et al. (1996) was based on very limited ripple measurements obtained at the beginning and/or end of field experiments and is far more from being tested. Fig. 7 shows that this formulation, just as other wave-ripple predictors of Nielsen (1981) and Grant and Madsen (1982), over-predicts ripple heights under combined flows and fails to include the effects of the enhancement of shear velocity by pre-existing ripples. Due to the complex non-linear interaction between waves and steady currents and the wide range of wave strengths relative to that of the steady current, we feel that a new empirical ripple predictor is needed for combined flows. Since it is the combined wave–current shear velocity that determines the overall ripple development under combined flows, the combined shear velocity should be used in this new predictor. Due to the importance of shear velocity enhancement by ripples when $u_{*cws} < u_{*cr}$, the new ripple predictor should properly predict the enhanced shear velocity at ripple crest, u_{*cwe}, and the resultant ripples under this condition. The ratios of u_{*ws}/u_{*cs} and ripple steepness η/λ are plotted in Fig. 8 as a function of time for the selected bursts in Table 1. Again the data points are connected with a solid line for clearer presentation, though they are not all consecutive. Ripple steepness varies from 0.07 to 0.15 for these bursts and co-varies with the relative strength of waves. Since these ripples are mostly in the equilibrium range in which ripple steepness should be roughly constant at the maximum and not effected by the magnitude of the shear stress, Fig. 8 thus suggests that ripple geometries can be significantly different under wave-dominant conditions than current-dominant conditions and therefore should be predicted separately.

When the average skin-friction combined shear velocity is less than the critical shear velocity ($u_{*cws} < u_{*cr}$) but ripple-enhanced shear velocity u_{*cwe} is larger than u_{*cr}, localized sediment transport occurs at the crests of ripples. We define this condition as the weak-transport range and the skin-friction combined shear velocity will be used

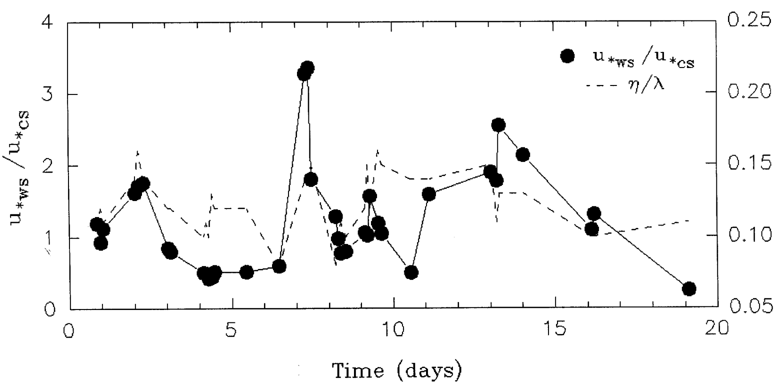

Fig. 8. The time series of measured ripple steepness, η/λ, compared with that of the ratio of skin-friction wave to current shear velocity, u_{*ws}/u_{*cs}, for selected bursts of the present study.

for ripple prediction in this range. The dimensionless ripple height, η/D is plotted in Fig. 9a against the normalized combined shear velocity, u_{*cws}/u_{*cr}, for ripples in the weak-transport range. A large scatter is evident, nevertheless, a least-square linear regression yields:

$$\eta/D = 19.6(u_{*cws}/u_{*cr}) + 20.9 \qquad (r^2 = 0.06) \tag{8}$$

Given the low r^2 value, the relationship of Eq. (8) is weak and it could as well be replaced by a constant of $\eta/D = 35$. Since the data in Fig. 9a does show a weak trend of increasing η with u_{*cws}, Eq. (8) will be used for further analyses of data. The steepness η/λ for these ripples are plotted against u_{*cws}/u_{*cr} in Fig. 9b with ripples being separated into current dominated (circles), wave dominated (squares) and combined wave–current ripples (triangles). This figure shows that η/λ for ripples in the weak-transport range is mainly determined by the relict ripple characteristics and cannot be predicted by the prevailing wave–current dynamics. Therefore, an average value of $\eta/\lambda = 0.12$ will be used to represent these ripples for the purpose of calculating BBL parameters.

In Table 1, thirteen ripple sets are in the equilibrium range (u_{*cws}/u_{*cr} and bedload shear velocity u_{*cwb} is smaller than the ripple breakoff shear velocity u_{*bf}) and two ripple sets are in the breakoff range ($u_{*cwb} \geqslant u_{*bf}$). Heights and steepness of these ripples are plotted against u_{*cwb} in Fig. 10a and b, respectively. The open circles represent wave-dominant ripples ($u_{*ws}/u_{*cs} \geqslant 1.25$), triangles represent combined wave–current ripples and solid circles represent ripples in the breakoff range. The vertical dashed line in Fig. 10a marks the ripple breakoff shear velocity of 3.23 cm/s. Fig. 10 shows that for a given shear velocity, both η and η/λ of the wave-dominant ripples are significantly higher than that of the combined wave–current ripples with the exception of one outlier (marked I) possibly due to measurement errors. No correlation between η/λ and u_{*cwb} is evident in Fig. 10b, but rather the data define that the average ripple steepness is 0.15 and 0.12 for the wave-dominant and combined wave–current ripples, respectively.

Wiberg and Harris (1994) recently compared various ripple expressions against laboratory and field wave ripple data and suggested that ripple length in the breakoff range (anorbital ripples) is proportional to the grain size: $\lambda = 535D$. Based on this expression, the average ripple length at the breakoff point and beyond should be 18.2 cm which roughly agrees with the maximum measured ripple length of 20 cm. If η/λ is taken to be 0.15 as defined in Fig. 10b, the possible maximum ripple height at the breakoff point will be 2.7 cm. This estimate is shown in Fig. 10a as a solid square and is in good agreement with the rest of the wave-dominant ripple data. Least-square linear regression has been performed separately for the two data groups in Fig. 10a to obtain:

$$\eta/D = 27.14(u_{*cwb}/u_{*cr}) + 16.36 \quad (r^2 = 0.69) \tag{9a}$$

for wave-dominant ripples, and

$$\eta/D = 22.15(u_{*cwb}/u_{*cr}) + 6.38 \quad (r^2 = 0.75) \tag{9b}$$

for combined wave–current ripples. The outlier was not used in obtaining Eq. (9b).

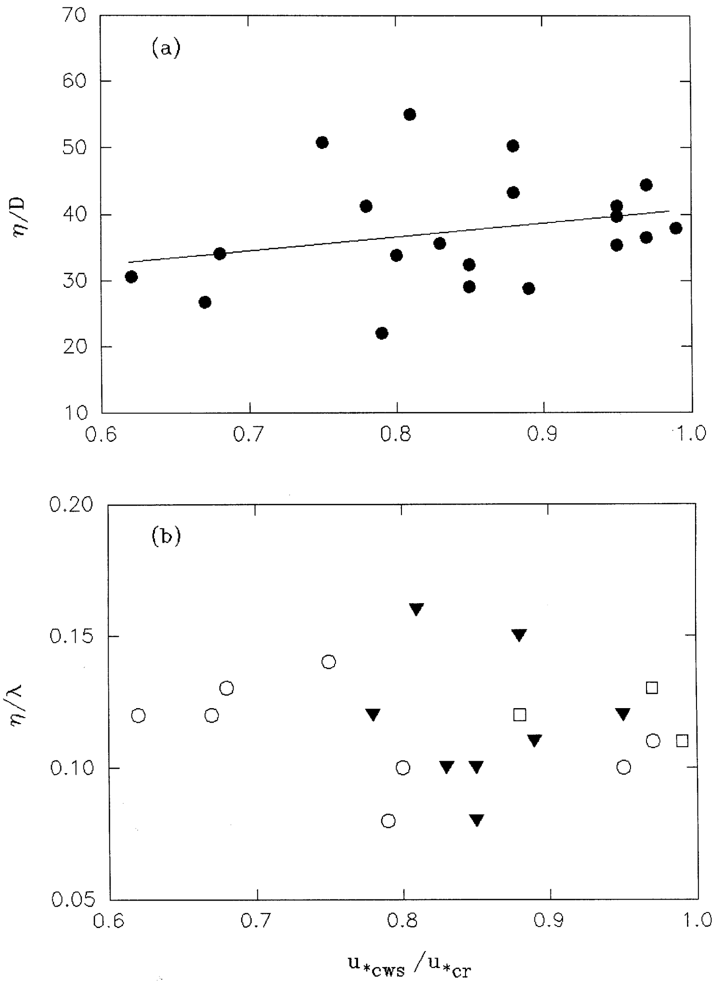

Fig. 9. Scatter plots of (a) the normalized ripple height, η/D, and (b) ripple steepness η/λ against the normalized skin-friction combined shear velocity, u_{*cws}/u_{*cr}, for ripples in the weak-transport range. The straight line in (a) is given by the least-squares linear regression Eq. (8). Circles, squares and triangles in (b) represent current-dominant, wave-dominant and combined wave-current ripples, respectively.

Fig. 10a also indicates that ripple heights will decrease with u_{*cwb} in the breakoff range. Unfortunately, we do not have enough data to derive a predictive expression. If we assume that ripple length stays roughly constant in the breakoff range and that the ripple steepness η/λ has the maximum value of 0.15 at the breakoff point and decreases to 0 when sheet flow condition is reached, then ripples in the breakoff range can be predicted by

$$\lambda = 535D \tag{10a}$$

$$\eta/\lambda = 0.15(u_{*up} - u_{*cwb})/(u_{*up} - u_{*bf}) \tag{10b}$$

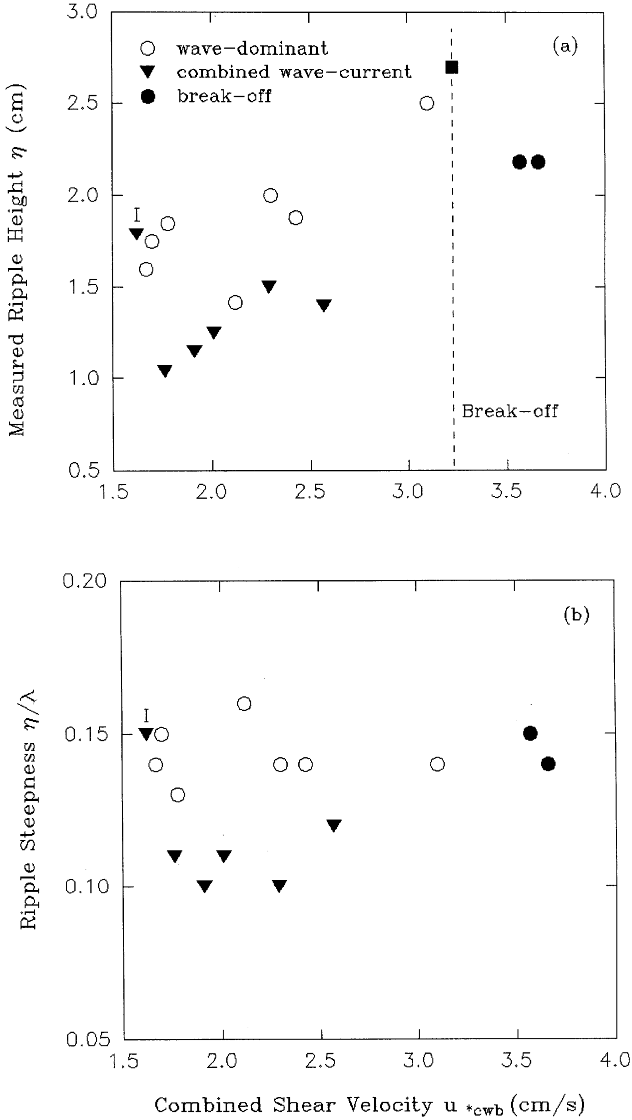

Fig. 10. Scatter plots of (a) measured ripple height η and (b) ripple steepness η/λ against the bedload combined shear velocity u_{*cwb} for ripples in the equilibrium and break-off ranges. The open circles and triangles represent wave-dominant and combined wave-current ripples, respectively, and the solid circles represent ripples in the break-off range. The solid square indicates the maximum possible ripple height at the break-off point and the dashed vertical line in (a) marks the ripple break-off shear velocity.

Eq. (10) predicts that when u_{*cwb} just reaches the ripple breakoff criterion u_{*bf}, ripple steepness will be at the maximum value of 0.15 and that as u_{*cwb} approaches the upper plane bed criterion u_{*up}, η/λ will approach zero. For $u_{*cwb} = 3.66$ cm/s, Eqs. (10a) and (10b) predict $\eta = 2.3$ cm which is close to the measured ripple height 2.2 cm (solid circles in Fig. 10a), providing qualitative support to Eqs. (10a) and (10b). However, more field measurements of breakoff ripples under combined flows are needed to test the applicability of Eqs. (10a) and (10b). For this reason, we suggest that the wave-ripple predictor of Nielsen (1981) or Wiberg and Harris (1994) could be used for predicting breakoff ripples under combined flows.

The proposed combined-flow ripple predictors (Eqs. (8)–(10)) are used to estimate ripple heights and ripple roughness heights from the data in Table 1. The predicted η and k_{br} are compared with measured values in Fig. 11. Although this is not an independent test of the method, it should show how well the proposed predictor fits the source data. The data points in Fig. 11 are again connected with a solid line for clearer presentation. Fig. 11 shows that as most of the ripples are in the weak-transport and equilibrium ranges, η and k_{br} generally increase with the combined shear velocity. The proposed expressions fit the source data reasonably well, suggesting that it can be used as a preliminary ripple predictor for combined flows. However, its general applicability can only be evaluated when more field data become available and independent tests of the predictor have been undertaken.

3.3. Bed roughness estimates

The total bed roughness height k_b is the sum of grain roughness height ($k_{bs} = 2.5D$), ripple roughness height (k_{br}) and bedload roughness height (k_{bt}): $k_b = k_{bs} + k_{br} + k_{bt}$ (Grant and Madsen, 1982). When sediment transport occurs, grain roughness becomes less important and the bed roughness is mainly determined by the presence of ripples and a bedload transport layer. In the following, we will briefly describe some of the ripple and bedload roughness height algorithms. The data of the present study will then be used to evaluate the applicability of these algorithms under combined flows.

Based on the work of Wooding et al. (1973) and other laboratory data, Grant and Madsen (1982) propose the following ripple roughness height expression:

$$k_{br} = 27.7\,\eta^2/\lambda \tag{11}$$

Based on the laboratory data of Carstens et al. (1969) and Lofquist (1986), Nielsen (1992) suggests a different expression:

$$k_{br} = 8\,\eta^2/\lambda \tag{12}$$

Both of these expressions are based on laboratory wave ripple data and their applicability to combined flows has not been tested.

Smith and McLean (1977), Dietrich (1982) and Grant and Madsen (1982) have developed different methods for the calculation of bedload roughness $z_{0t}(=k_{bb}/30)$. Based on unidirectional-flow flume data, Wiberg and Rubin (1989) and Li (1994) find that both Smith and McLean and Grant and Madsen over-predict z_{0t}, and that only Dietrich's expression agrees with the flume data. However, Nielsen

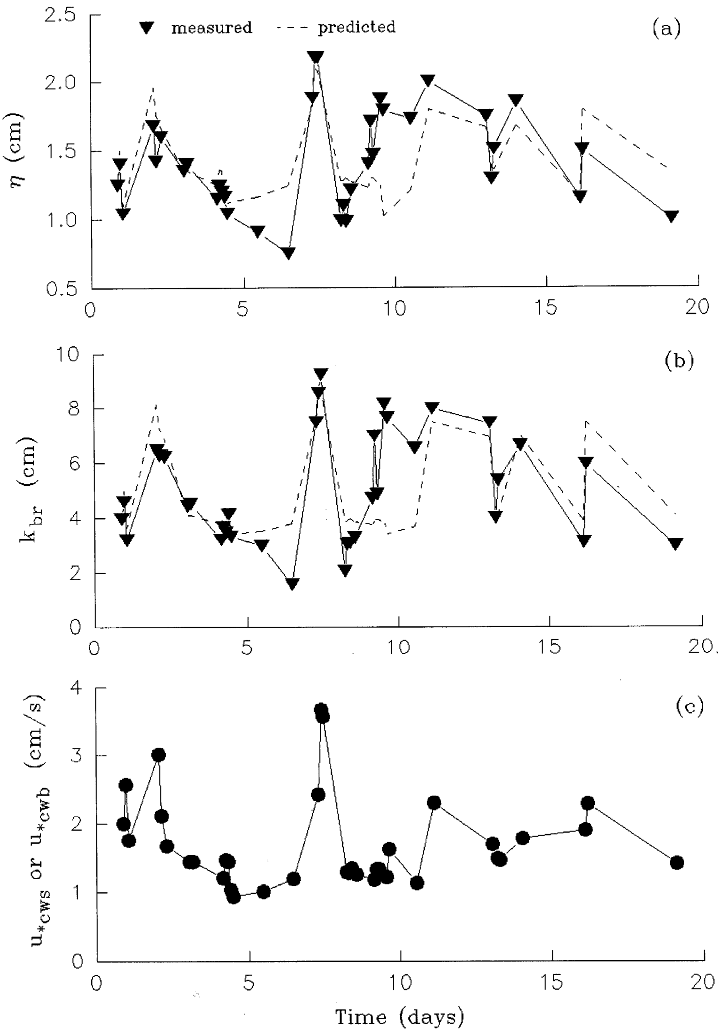

Fig. 11. Time series of (a) the measured ripple height η, (b) ripple roughness height k_{br} and (c) skin-friction or bedload combined shear velocity (u_{*cws} or u_{*cwb}) for selected bursts. The dashed lines in (a) and (b) represent the predicted ripple height and ripple roughness height by the proposed empirical ripple predictor for combined flows.

(1992) demonstrates that bedload roughness under waves is about one order of magnitude higher than that under unidirectional flows.

Based on the vertical particle momentum equation and the laboratory oscillatory flow data of Carstens et al. (1969), Grant and Madsen (1982) found:

$$h_{tm} = 42(\rho_s/\rho + 0.5)D\theta_{cr}[(\theta_{cws}/\theta_{cr})^{0.5} - 0.7]^2 \tag{13a}$$

$$k_{bt} = 3.8\, h_{tm} \tag{13b}$$

where h_{tm} is the thickness scale of the bedload layer, $\theta_{cws} = \rho u_{*cws}^2/(\rho_s - \rho)gD$ is the skin-friction combined Shields parameter. Wiberg and Rubin (1989) used the steady-flow flume data of Guy et al. (1966) and a function proposed by Dietrich (1982) to derive the following:

$$h_{tm} = 0.68\,\tau_*/(1 + a_2\,\tau_*) \tag{14a}$$

$$k_{bt} = 1.68\,h_{tm} \tag{14b}$$

where $\tau_* = (u_{*cws}/u_{*cr})^2$ is the normalized shear stress and a_2 is a grain-size-related coefficient given by $a_2 = 0.0204(\ln D)^2 + 0.022\ln D + 0.0709$. Also based on the flat-bed oscillatory flow data of Carstens et al. (1969), Nielsen (1992) suggests:

$$k_{bt} = 170\,D(\theta_{cws} - \theta_{cr})^{0.5} \tag{15}$$

Upper-plane bed sheet flow was observed during the three major storms. Following Wilson (1988) and Wiberg and Harris (1994), we believe that the friction factor under sheet flow conditions is determined predominantly by the presence of the bedload transport layer. The first burst in which the sheet flow was observed in each storm was chosen to represent the onset of sheet flow under combined waves and current. The various bedload roughness algorithms were used in the GM86 model to predict the bedload shear velocity u_{*cwb} for these bursts which were then compared against the established critical shear velocity $u_{*up} = 5.8$ cm/s for sheet flow (Komar and Miller, 1975) to evaluate the applicability of these algorithms under combined flows. The model-predicted bedload shear velocities are plotted in Fig. 12 for these sheet-flow bursts in which the bedload roughness algorithms of Wiberg and Rubin (WR, 1989), Grant and Madsen (GM, 1982) and Nielsen (NL, 1992) are represented, respectively, by squares, circles, and triangles. The dashed line indicates the critical shear velocity for sheet flow $u_{*up} = 5.8$ cm/s. Fig. 12 shows that the bedload shear velocities based on the bedload roughness algorithm of Wiberg and Rubin (1989) are significantly smaller than the established u_{*up} value, indicating under-estimation of bedload roughness by Wiberg and Rubin (1989) under combined flows. Nielsen (1992) demonstrates that for a given bed shear stress, the bedload roughness height under waves is about one order of magnitude higher than that under unidirectional flows. Thus the under-estimation of bedload roughness by the algorithm of Wiberg and Rubin (1989) must be due to the fact that their algorithm was based on the unidirectional flume data of Guy et al. (1966). The bedload shear velocities predicted using the bedload roughness algorithms of Nielsen (1992) and Grant and Madsen (1982) seem to reasonably agree with $u_{*up} = 5.8$ cm/s (Fig. 12), suggesting their general applicability under combined flows. However, the thickness scale of the bedload layer, h_{tm}, predicted by the algorithm of Grant and Madsen (1982) was found more than an order of magnitude higher than the wave tunnel measurements of Sawamoto and Yamashita (1986; The only direct laboratory measurements of bedload layer thickness under waves we are aware of). Therefore, the bedload roughness algorithm of Grant and Madsen (1982) must be used with caution.

Based on the same observed sheet-flow data as presented here and the wave tunnel measurements of Sawamoto and Yamashita (1986), Li et al. (1997) adjusted the

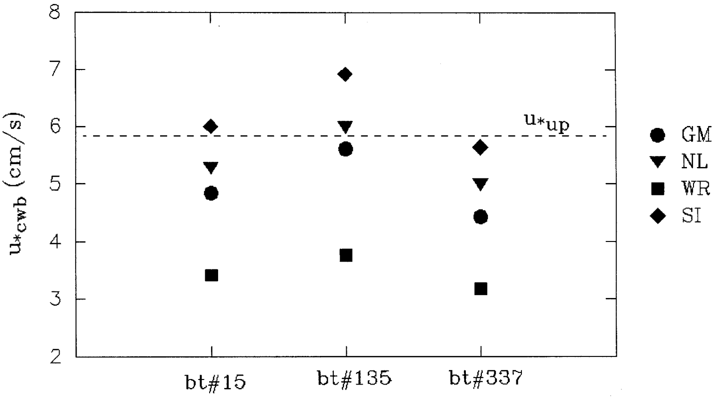

Fig. 12. Bedload shear velocities predicted for the selected bursts representing the onset of upper-plane bed sheet flow during storms. The symbols of squares, circles, triangles and diamonds represent predictions using the bedload roughness algorithms of Wiberg and Rubin (1989, WR), Grant and Madsen (1982, GM), Nielsen (1992, NL), and Li et al. (1997). The dashed line indicates the established critical shear velocity for sheet flow $u_{*up} = 5.8$ cm/s.

proportionality between k_{bt} and h_{tm} to best match the predicted bedload shear velocity u_{*cwb} with $u_{*up} = 5.8$ cm/s and derived the following bedload roughness algorithm for combined flows:

$$h_{tm} = 2.9D(\theta_{cws} - \theta_{cr})^{0.75} \tag{16a}$$

$$k_{bt} = 180h_{tm} \tag{16b}$$

The predicted bedload shear velocity u_{*cwb} using Eqs. (16a) and (16b) are plotted in Fig. 12 as diamonds for comparison with predictions from other bedload roughness algorithms, though this obviously is not an independent testing of the bedload roughness algorithm of Li et al. (1997).

In order to evaluate the ripple roughness algorithms given in Eqs. (11) and (12), the total current shear velocity, u_{*c}, and the apparent bottom roughness, z_{0c}, should be obtained from linear regression of the velocity profiles and then compared with the predicted values from the GM86 model using these ripple roughness height algorithms. Since velocity was measured at only two heights (50 and 100 cm) in this study, we have to use a simplified logarithmic velocity profile method (Sternberg, 1972) to derive u_{*c} and z_{0c}:

$$u_{*c} = (u_{100} - u_{50})/[5.75(\log 100 - \log 50)] \tag{17a}$$

$$z_{0c} = \exp(4.61 - 0.4u_{100}/u_{*c}) \tag{17b}$$

where u_{50} is the mean velocity measured at 50 cm above the sea bed. Large errors could be associated with these estimates due to, among other factors, bed elevation changes and the influences of internal waves. But given the scarcity of simultaneous measurements of wave-current dynamics and ripple geometry under combined flow condition, we favor the use of the data to provide a preliminary evaluation of the applicability of various ripple and bedload roughness algorithms to combined flows and hope this will serve as a start for further studies. Seabed photos show that the shadow bar became partially buried about 2.5 days into the experiment. This suggests that bed elevation after that changed significantly from the initial level. This caused unreasonable high values of the observed u_{*c} and z_{0c} from Eqs. (17a) and (17b) based on measured u_{50} and u_{100}. The values of the observed u_{*c} and z_{0c} often reached more than 5 cm/s and 20 cm, respectively. It is thus impossible to use the whole data set to evaluate the various ripple and bedload roughness height algorithms. Therefore, only the data from the first 2.5 days (about 31 bursts), for which we knew that seabed elevation changes were minimum, were used in the evaluation of various ripple and bedload roughness height algorithms. Large wave ripples were observed in four of the chosen 31 bursts. Since our current understanding of LWR development is not enough to warrant their prediction, they were not used in the evaluation. Of the remaining 27 bursts, 15 bursts are in the no motion or weak-transport condition. Bed roughness was thus predominantly due to the existence of ripples for these bursts. The measured ripple heights and lengths for these 15 bursts were used in the GM86 model to predict total current shear velocity u_{*c} and apparent bed roughness z_{0c} respectively. The velocity measurements u_{50} and u_{100} were then used in Eqs. (17a) and (17b) to obtain the 'observed' u_{*c} and z_{0c}. The predicted and observed u_{*c} and z_{0c} are compared in Fig. 13 to evaluate the applicability of these ripple roughness height algorithms under combined flows. Ripple roughness height algorithm of Grant and Madsen (1982) was used in Fig. 13a and c, and the algorithm of Nielson (1992) was used in Fig. 13b and d. Circles and triangles in Fig. 13 represent no transport and weak transport conditions, respectively. The dashed lines in Fig. 13 indicate the perfect agreement. Plots in Fig. 13 show that the ripple roughness height algorithm of Grant and Madsen (1982) gives reasonable predictions of u_{*c} and z_{0c} under combined flows and that the ripple roughness height algorithm of Nielsen (1992) causes under-predictions of u_{*c} and z_{0c}.

Of the chosen 31 bursts at the beginning of the deployment, active ripples were observed in 10 bursts and sheet flow occurred in two bursts. Measured ripple heights and lengths of these bursts and the ripple roughness height algorithm of Grant and Madsen (1982) were used in GM86 model to predict total current shear velocity u_{*c} and apparent bed roughness z_{0c} based on various bedload roughness algorithms. Predicted u_{*c} and z_{0c} are compared with the observed u_{*c} and z_{0c} (again calculated from Eqs. (17a) and (17b) based on measured velocity at 50 and 100 cm above seabed) in Figs. 14 and 15 in order to further evaluate the applicability of various bedload roughness algorithms. In Figs. 14 and 15, (a) is based on the bedload roughness algorithm of Grant and Madsen (1982), (b) Nielsen (1992), (c) Wiberg and Rubin (1989) and (d) Li et al. (1997). The two triangles represent the two sheet-flow bursts and the dashed lines again indicate the perfect fit. Thought sediment transport occurred in the bursts of active ripples (circles in Fig. 14), ripple roughness was still dominant over bedload transport roughness and values of the predicted u_{*c} are overwhelmingly dictated by the proper prediction of the ripple roughness height algorithm of Grant and Madsen (1982). Thus all the bedload roughness algorithms seem to give reasonable prediction of u_{*c}. Ripples were washed out in the two sheet-flow bursts (triangles in Fig. 14) and the bed roughness should be purely due to

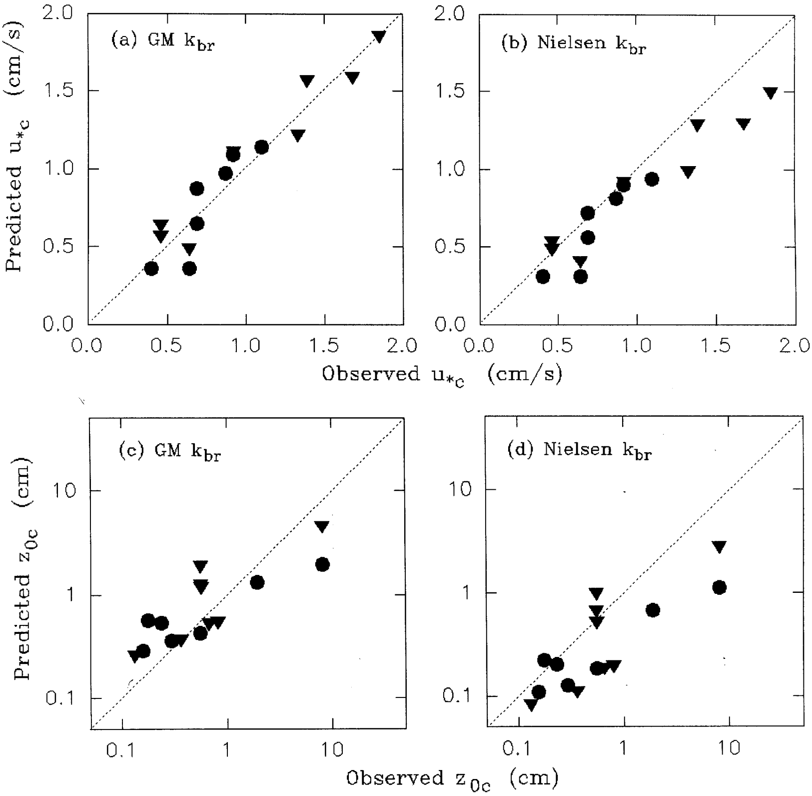

Fig. 13. Predicted and observed total current shear velocity, u_{*c}, and apparent bottom roughness, z_{0c}, for no-transport bursts (circles) and weak-transport bursts (triangles). The ripple roughness height algorithms of Grant and Madsen (1982) was used in (a, c) and that of Nielsen (1992) was used in (b, d). The dashed lines indicate perfect agreement.

bedload transport. The comparison of predicted and observed u_{*c} for these two bursts, however, seem to indicate that the bedload roughness algorithms of Nielsen (1992) and Li et al. (1997) better predict u_{*c} under combined flows and that the algorithms of Grant and Madsen and Wiberg and Rubin tend to under-predict for combined flows. The comparison between the observed and predicted apparent bottom roughness z_{0c} in Fig. 15 seem to further support this conclusion. Given the uncertainty in the observed u_{*c} and z_{0c}, however, this conclusion is preliminary at the best and needs to be tested with better field data in which both bedforms and complete velocity profiles have to be measured.

4. Summary and conclusions

The development of ripples, the initiation of sheet flow and their associated bed roughnesses under combined flows are complex and critical issues for modelling

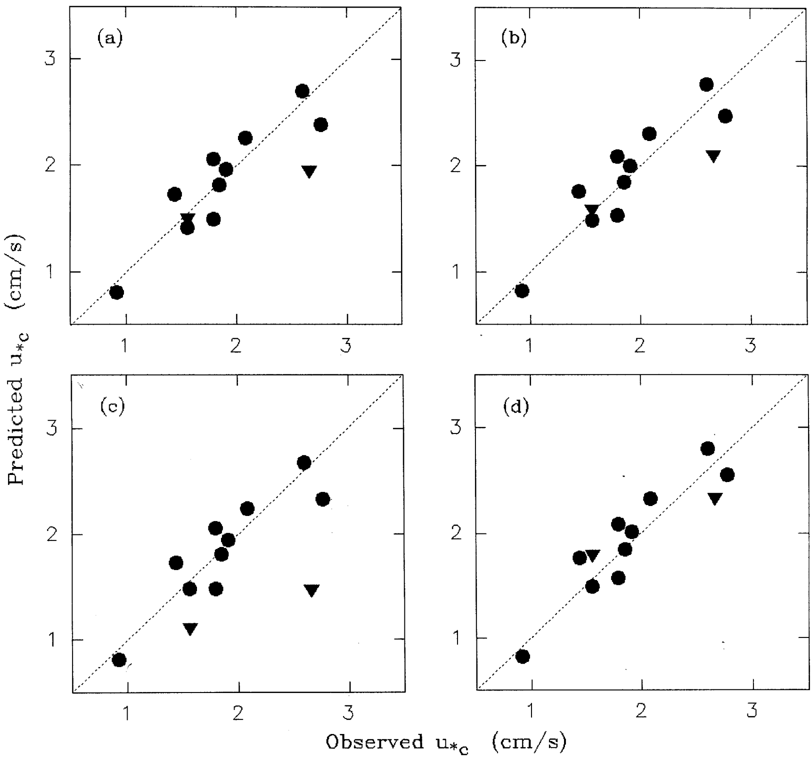

Fig. 14. Scatter plots of the observed and predicted total current shear velocity u_{*c} for sediment-transport bursts. Various bedload roughness algorithms were used: (a) Grant and Madsen (1982), (b) Nielsen (1992), (c) Wiberg and Rubin (1989) and (d) Li et al. (1997). Circles represent bursts in which both ripples and bedload transport were observed, and triangles represent sheet-flow bursts. Dashed lines indicate perfect fits.

boundary layer dynamics and sediment transport on continental shelves. The data collected from Sable Island Bank, together with the predictions of the Grant and Madsen's (1986) combined-flow BBL model, indicate that a variety of ripple types exist on continental shelves due to variable wave strengths relative to that of the current. Wave-dominant ripples, formed during storms, differ from current-dominant ripples in their shape and crest-line pattern. They are also higher and steeper under a given bed shear stress. Amos et al. (1988) showed that various ripple types can be separated using partitioned current and wave Shields parameters. This study further proves that the ratios of the skin-friction wave to current shear velocity, u_{*ws}/u_{*cs}, can be used to separate combined-flow ripples into wave-dominant ($u_{*ws}/u_{*cs} > 1.25$), current dominant ($u_{*ws}/u_{*cs} < 0.75$) and combined wave-current ($0.75 < u_{*ws}/u_{*cs} < 1.25$) ripples.

The comparison of the measured ripple height and wavelength with the predictions by the wave-ripple predictors of Nielsen (1981) and Grant and Madsen (1982) indicates that both methods significantly over-predict ripple height and ripple

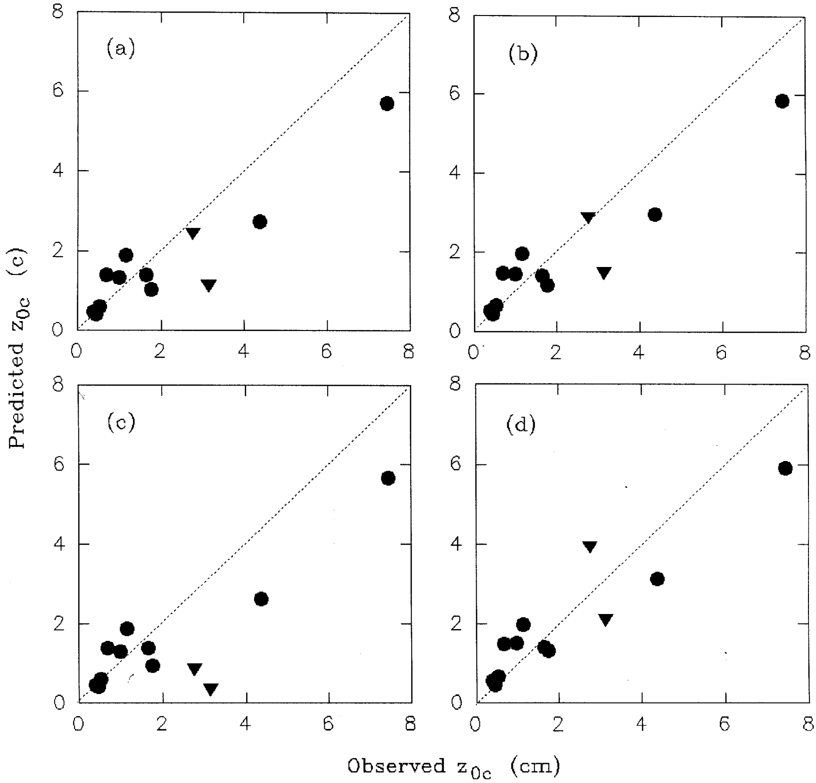

Fig. 15. Scatter plots of the observed and predicted apparent bottom roughness z_{0c} for sediment-transport bursts. Various bedload roughness algorithms were used: (a) Grant and Madsen (1982), (b) Nielsen (1992), (c) Wiberg and Rubin (1989) and (d) Li et al. (1997). Circles represent bursts in which both ripples and bedload transport were observed, and triangles represent sheet-flow bursts. Dashed lines indicate perfect fits.

roughness for combined flows under the conditions of the present study. These methods also neglect the effect of the enhanced shear stress at the ripple crest; thus they predict no-transport flat beds when active ripples were observed in the field. Based on the measured ripple geometry and dynamic transition of ripples observed on the Scotian Shelf, a new empirical ripple predictor has been proposed for combined flows (Eqs. (8)–(10b)). The combined shear velocity and the ratio of wave shear velocity to current shear velocity are used in this new predictor to predict ripple types, geometry and their dynamic transitions under combined flows. The effect of enhanced shear velocity at the ripple crest is also incorporated in this method to properly predict ripples in the weak-transport range. The comparison between field ripple measurements and the predictions of this new ripple predictor shows good agreement, but its general applicability needs to be tested by more field data covering different grain sizes. Large wave ripples were observed to form immediately following sheet flow conditions during the waning periods of storms. These ripples, usually 5–7 cm in height and 60–70 cm in wavelength, can significantly change the bottom roughness, bed shear-stress and nearbed velocity profiles. Thus their formation mechanism needs to be studied and a predictive algorithm of their geometry should be added to the proposed new ripple predictor.

A simplified logarithmic profile method and the values of the bedload shear velocities predicted for the sheet-flow bursts were used to evaluate the applicability of various ripple- and bedload-roughness height algorithms under the combined flow condition. The ripple roughness height algorithm of Grant and Madsen (1982) was found to give good predictions of total current shear velocity u_{*c} and apparent bottom roughness z_{0c}. The ripple roughness height algorithm of Nielsen (1992) was found to under-predict u_{*c}, and z_{0c}. The bedload roughness algorithm of Nielsen (1992) was found applicable under combined flows. The steady- current bedload roughness algorithm of Wiberg and Rubin (1989) significantly under-estimates bedload roughness under combined flows. Though the application of the bedload roughness algorithm of Grant and Madsen (1982) seemed to give fair predictions of the bedload shear velocity, it over-estimates the scale of the bedload layer thickness by one order of magnitude and caution must be exercised to use it in the GM86 model. In general, the following equation can be used to predict the total bed roughness height under combined flows:

$$k_b = 2.5D + 27.7\eta^2/\lambda + 170D(\theta_{cws} - \theta_{cr})^{0.5} \tag{18}$$

with the last part being obtained from Eq. (15).

Acknowledgements

The authors would like to thank David Heffler, John Zevenhuizen and Bruce Wile for instrumentation and field assistance during this project, and Robert Courtney for help in using GRASS for seabed photo analysis. We also appreciate the corporation of LASMO Nova Scotia Ltd. during the field work. Steve Solomon and Thierry Mulder critically reviewed the manuscript of this paper. The critics from two journal reviewers significantly improved this paper. The funding for this work was provided by the Panel on Energy Research and Development (PERD) of the Federal Government of Canada through Offshore Geotechnics Program 63204. Geological Survey of Canada Contribution Number 26595.

References

Allen, J.R.L., 1968. Current Ripples. Their Relationship to Patterns of Water and Sediment Motion. North-Holland, Amsterdam, 433 pp.

Allen, J.R.L., 1982. Sedimentary Structures. Their Character and Physical Basis. 2 vols. Elsevier, Amsterdam, 593 pp, 663 pp.

Amos, C.L., Nadeau, O.C., 1988. Surficial sediments of the outer banks, Scotian Shelf, Canada. Canadian Journal of Earth Sciences 25(12), 1923–1944.

Amos, C.L., Bowen, A.J., Huntley, D.A., Lewis, C.F.M., 1988. Ripple generation under the combined influences of waves and currents on the Canadian continental shelf. Continental Shelf Research 8, 1129–1153.

Bagnold, R.A., 1956. Flow of cohesionless grains in fluids. Philosophical Transactions of the Royal Society of London A249, 235–297.

Boyd, R., Forbes, D.L., Heffler, D.E., 1988. Time-sequence observations of wave-formed sand ripples on an ocean shoreface. Sedimentology 35, 449–464.

Carstens, M.R., Neilson, R.M., Altinbilek, H.D., 1969. Bedforms generated in the laboratory under oscillatory flow: analytical and experimental study. U.S. Army Corps of Engineers, Coastal Engineering Research Center, Technical Memorandum 28, 39 pp.

Dietrich, W.D., 1982. Flow, boundary shear stress and sediment transport in a river meander. Ph.D. Dissertation, University of Washington, Seattle, 261 pp.

Dingler, J.R., 1974. Wave formed ripples in nearshore sands. Ph.D Thesis, University of California, San Diego, 136 pp.

Drake, D.E., Cacchione, D.A., 1989. Estimates of the suspended sediment reference concentration (C_a) and resuspension coefficient (γ) from near-bed observations on the California shelf. Continental Shelf Research 9, 51–64.

Drake, D.E., Cacchione, D.A., 1992. Wave-current interaction in the bottom boundary layer during storm and non-storm conditions: observations and model predictions. Continental Shelf Research 12, 1331–1352.

Glenn, S.M., Grant, W.D., 1987. A suspended sediment stratification correction for combined wave and current flows. Journal of Geophysical Research 92, 8244–8264.

Grant, W.D., Madsen, O.S., 1979. Combined wave and current interaction with a rough bottom. Journal of Geophysical Research 84, 1797–1808.

Grant, W.D., Madsen, O.S., 1982. Moveable bed roughness in unsteady oscillatory flow. Journal of Geophysical Research 87, 469–481.

Grant, W.D., Madsen, O.S., 1986. The continental shelf bottom boundary layer. Annual Review of Fluid Mechanics 18, 265–305.

Guy, H.P., Simons, D.B., Richardson, E.V., 1966. Summary of alluvial channel data from flume experiments, 1956–1961. USGS Prof. Paper 462–I, Washington D.C., 96 pp.

Heffler, D.E., 1984. RALPH - An instrument to monitor seabed sediments. Current Research Part B, Geological Survey of Canada Paper 84-1b, pp. 47–52.

Inman, D.L., 1957. Wave-generated ripples in nearshore sands. U.S. Army Corps Engineers, Beach Erosion Board, Tech. Memo. 100, Washington, D.C., 66 pp.

Komar, P.D., Miller, M.C., 1975. The initiation of oscillatory ripple marks and the development of plane-bed at high shear stresses under waves. Journal of Sedimentary Petrology 45, 697–703.

Li, M.Z., 1994. Direct skin friction measurements and stress partitioning over movable sand ripples. Journal of Geophysical Research 99, 791–799.

Li, M.Z., Wright, L.D., Amos C.L., 1996. Predicting ripple roughness and sand resuspension under combined flows in a shoreface environment. Marine Geology 130, 139–161.

Li, M.Z., Amos, C.L., Heffler, D.E., 1997. Boundary layer dynamics and sediment transport under storm and non-storm conditions on the Scotian shelf. Marine Geology 141, 157–181.

Lofquist, K.E.B., 1986. Drag on naturally rippled beds under oscillatory flows. Miscellaneous Paper, CERC-86-13.

Madsen, O.S., Wright, L.D., Boon, J.D., Chisholm, T.A., 1993. Wind stress, bed roughness and sediment suspension on the inner shelf during an extreme storm event. Continental Shelf Research 13, 1303–1324.

Manohar, M., 1955. Mechanics of bottom sediment movement due to wave action. U.S. Army Corps Engineers, Beach Erosion Board, Tech. Memo. 75, Washington, D.C., 121 pp.

Miller, M.C., Komar, P.D., 1980. A field investigation of the relationship between oscillation ripple spacing and the near-bottom water orbital motion. Journal of Sedimentary Petrology 50, 183–191.

Miller, M.C., McCave, I.N., Komar, P.D., 1977. Threshold of sediment motion under unidirectional currents. Sedimentology 24, 507–527.

Mobil Oil Canada Ltd., 1983. Venture Development Project Environmental Impact Statement, vol. IIa, Biophysical Assessment. Mobile Oil Canada Ltd., Canadian Oil and Gas Lands Administration, Ottawa, 415 pp.

Mogridge, G.R., Kamphuis, J.W., 1972. Experiments on bed-form generation by wave action. In: Proceedings of the 13th Coastal Engineering Conf., ASCE, Vancouver, pp. 1123–1142.
Nielsen, P., 1981. Dynamics and geometry of wave-generated ripples. Journal of Geophysical Research 86, 6467–6472.
Nielsen, P., 1986. Suspended sediment concentrations under waves. Coastal Engineering 10, 23–31.
Nielsen, P., 1992. Coastal bottom boundary layers and sediment transport. Advanced Series on Ocean Eng. vol. 4. World Scientific, Singapore, pp. 324.
Owen, P.R., 1964. Saltation of uniform grains in air. Journal of Fluid Mechanics 20, 225–242.
Reineck, H.E., Singh, I.B., 1975. Depositional Sedimentary Environments. Springer, Amsterdam, 439 pp.
Ribberink, J.S., Al-Salem, A.A., 1994. Sediment transport in oscillatory boundary layers in cases of rippled beds and sheet flow. Journal of Geophysical Research 99, 12,707–12,727.
Sawamoto, M., Yamashita, T., 1986. Sediment transport rate due to wave action. Journal of Hydroscience and Hydraulic Engineering 4, 1–15.
Smith, J.D., 1977. Modelling of sediment transport on continental shelves. In: Goldberg et al., E.D. (Eds), The Sea, vol. 6. Wiley-Interscience, New York, pp. 539–577.
Smith, J.D., McLean, S.R., 1977. Boundary layer adjustments to bottom topography and suspended sediments. In: Nihoul, J.C.J. (Ed.), Botto Turbulence. Elsevier, New York, pp. 123–151.
Sternberg, R.W., 1972. Predicting initial motion and bedload transport of sediment particles in the shallow marine environment. In: Swift, D.J.P., Duane, D.B., Pilkey, O.H. (Eds), Shelf Sediment Transport: Process and Pattern. Dowden, Hutchnison and Ross, Stroudsburg, PA., pp. 61–82.
Vincent, C.E., Hanes, D.M., Bowen, A.J., 1991. Acoustic measurements of suspended sand on the shoreface and the control of concentration by bed roughness. Marine Geology 96, 1–18.
Wiberg, P.L., Rubin, D.M., 1989. Bed roughness produced by saltating sediment. Journal of Geophysical Research 94, 5011–5016.
Wiberg, P.L., Nelson, J.M., 1992. Unidirectional flow over asymmetric and symmetric ripples. Journal of Geophysical Research 97, 12,745–12,761.
Wiberg, P.L., Harris, C.K., 1994. Ripples geometry in wave-dominated environments. Journal of Geophysical Research 99, 775–789.
Wilson, K.C., 1988. Mobile-bed friction at high shear stress. Journal of Hydraulic Engineering ASCE 115(6), 825–830.
Wilson, K.C., 1989. Friction of wave-induced sheet flow. Coastal Engineering 12, 371–379.
Wooding, R.A., Bradley, E.F., Marshall, J.K., 1973. Drag due to regular arrays of roughness elements of varying geometry. Boundary Layer Meteorology 5, 285–308.
Wright, L.D., Boon, J.D., Green, M.O., List, J.H., 1986. Response of the mid-shoreface of the southern mid-Atlantic Bight to a "Northeaster". Geo-Marine Letters 6, 153–160.

Notation

A_b	near-bed wave orbital amplitude
C_{dir}	direction of mean current
D	median grain diameter of sediment
g	gravity acceleration
h	water depth
H_s	significant wave height
h_{tm}	thickness scale of bedload layer
k_b	total bed roughness height
k_{br}	ripple roughness height
k_{bs}	sediment grain roughness height
k_{bt}	bedload transport roughness height
M	wave mobility number
R_m	ripple migration rate

S_*	dimensionless sediment parameter
T	wave period
u_b	nearbed wave orbital velocity
u_{50}	mean velocity at 50 cm above the bottom
u_{100}	mean velocity at 100 cm above the bottom
u_{*bf}	critical shear velocity for ripple breakoff
u_{*c}	total current shear velocity
u_{*cr}	critical shear velocity for bedload transport
u_{*cs}	skin-friction current shear velocity based on grain roughness only
u_{*cwb}	bedload shear velocity based on combined grain and bedload roughnesses
u_{*cwe}	ripple enhanced shear velocity
u_{*cws}	skin-friction combined shear velocity based on grain roughness only
u_{*s}	critical shear velocity for sediment suspension
u_{*ws}	skin-friction wave shear velocity based on grain roughness only
u_{*up}	critical shear velocity for upper-plane bed sheet flow
W_{dir}	propagation direction of waves
z_{0c}	apparent bottom roughness
z_{0t}	bedload transport roughness
η	ripple height
λ	ripple wavelength
η/λ	ripple steepness
θ_{bf}	critical Shields parameter for ripple breakoff
θ_{cr}	critical Shields parameter for bedload transport
θ_{cws}	skin-friction combined Shields parameter
θ_{up}	critical Shields parameter for upper-plane bed sheet flow
θ_{ws}	skin-friction wave Shields parameter
v	kinematic fluid viscosity
ρ	fluid density
ρ_s	sediment density
τ_*	normalized excess shear stress